Electrodeposition, Microstructure and Magnetic Properties of Nickel-Cobalt-Copper Alloy Powders

0013-4651/2018/165(11)/D511/7/$37.00 © The Electrochemical Society

Electrodeposition, Microstructure and Magnetic Properties of Nickel-Cobalt-Copper Alloy Powders

Miroslav Spasojević,[1] Milica Spasojević,[2,z] Pavle Mašković,[1] Dušan Marković,[1] and Lenka Ribić-Zelenović[1]

[1] *Joint Laboratory for Advanced Materials of SASA, Section for Amorphous Systems, Faculty of Technical Sciences, Čačak, University of Kragujevac, Čačak, Serbia*
[2] *Faculty of Chemistry, University of Belgrade, Belgrade, Serbia*

Powders of Ni-Co alloys containing small amounts of Cu were produced by electrodeposition from an ammonium bath. Cathodic polarization curves were recorded and partial current densities for alloy deposition and hydrogen evolution were determined. At a current density of 100 mA cm^{-2}, the electrodeposition process resulted in $Ni_{79.1}Co_{18.6}Cu_{2.3}$ powder with an average grain size of 6.8 nm, composed of an amorphous matrix and FCC nanocrystals. The deposition of Cu with Ni and Co led to a higher proportion of the amorphous phase, smaller nanocrystals and smaller powder particles in the electrodeposit than in the alloy without copper. During annealing at temperatures ranging from 25°C to 160°C, no structural changes occurred in the powder. Upon structural relaxation in the temperature range of 160–350°C, the powders cooled at 25°C showed greater magnetic permeability. At temperatures between 350°C and 430°C, the amorphous phase exhibiting relatively lower magnetization underwent crystallization, accompanied by the formation of small-sized FCC nanocrystals, which had relatively higher magnetization values, leading to an increase in the magnetic permeability of the cooled powder. At temperatures above 430°C, the formation of large crystalline grains at the expense of small ones caused a decrease in magnetization.
 [DOI: 10.1149/2.0441811jes]

Manuscript submitted June 25, 2018; revised manuscript received July 31, 2018. Published August 14, 2018.

Owing to their specific physical and chemical properties, nanostructured materials are extensively used in a wide range of technologies such as preparation of composite nanofibers encapsulated with nanostructured materials, novel nanosensors and new packaging materials, new membranes with antimicrobial properties, polymer composite materials for biomedical applications etc.[1–5] Nanostructured nickel-cobalt alloys have good mechanical, electrical and magnetic properties, and exhibit high values of thermal, stability, wear resistance, corrosion resistance and catalytic activity for some electrochemical reactions. Ferromagnetic nickel-cobalt alloy powders are widely applied in conductive inks, magnetic fluids, and high density recording materials.[6] Fine particles of nickel-cobalt alloys, when dispersed in an insulating material, exhibit resonant absorption in the microwave region,[7] which may lead to their use as electromagnetic absorbers. F. Fievet et al.[8,9] have shown that nickel-cobalt alloy powders having the desired particle size can be obtained through the polyol process, in which the nucleation and growth of metal particles from simple salts such as hydroxides or acetates are controlled using ethylene glycol or diethylene glycol. P. Toneguzzo[10] has synthesized sub-micron and nanosized particles of nickel-cobalt alloys from a mixture of acetates in the presence of sodium hydroxide and a small concentration of silver nitrate or chloroplatinic acid. K. V. M. Shafi et al.[11] have reported the synthesis of nanosized amorphous powders of $Ni_{80}Co_{20}$ and $Ni_{50}Co_{50}$ by sonochemical decomposition of $Co(NO)(CO)_3$ and $Ni(CO)_4$ in decalin. Y. D. Li. et al.[12] have produced $Co_{(1-x)}Ni_x$ ($0 \leq x \leq 1$) alloys by a hydrothermal reduction method. P. Elumalai et al.[13] have obtained sub-micron sized (0.2–0.6 μm) particles of $Co_{(1-x)}Ni_x$ alloys of uniform composition, comprising largely non-agglomerated particles, using malonates as precursors. Xian-Ming Liu et al.[14] have synthesized $Ni_{50}Co_{50}$ particles ranging in size from 200 nm to 500 nm by reduction with ethylene glycol nickel and cobalt acetates. Alloy powder crystallites were composed of the FCC-structured solid solution of cobalt and nickel. The magnetic properties (saturation magnetization and coercivity) were determined. The electrochemical generation of nickel-cobalt alloys is a simple and relatively inexpensive process. Most studies focus on the production of compact coatings.[15–37] However, there are studies evaluating the electrodeposition and characteristics of nickel-cobalt powders.[38–50] The deposition of small amounts of copper with iron group metals ensures the obtainment of powders having an appropriate mean particle size, nanosized crystalline grains, good magnetic properties and high corrosion resistance.[51–60] Electrodeposited ternary nickel-cobalt-copper alloys are used as magnetic or magnetoresistive materials, which have better corrosion resistance than the Co–Cu system.[51–58]

Nanostructured alloys occur in a metastable state. Annealing these alloys at elevated temperatures leads to heat-induced changes in their microstructure, which consequently affect their physical and chemical properties.[46–48,59,60] Annealing nanostructured alloys at temperatures below the crystallization temperature results in their structural relaxation, which involves short-range ordering.[46–48,59,60] At higher temperatures, amorphous phase crystallization and crystal grain growth take place, leading to changes in the mechanical, electrical, magnetic and corrosion properties of the alloy.[46–48,59,60]

The objective of this experiment was to examine the effect of the deposition of small amounts of copper with nickel and cobalt on the chemical composition, morphology and microstructure of electrodeposited Ni-Co-Cu alloys, and to evaluate the effect of these properties and annealing temperature on magnetic characteristics.

Experimental

The electrodeposition of the nickel-cobalt-copper alloy was performed in a 2.5 dm^3 glass electrochemical cell. The cell contained a saturated mercury sulfate electrode used as the reference electrode connected via the Luggin capillary. The anode was a flat platinum mesh with a geometric surface area of 16 cm^2 (4 cm × 4 cm), and the cathode was a titanium plate of 4.2 cm^2 surface area and 0.3 cm width placed in parallel to the anode. The cell was placed in the thermostat. The operating temperature was 27 ± 0.5°C. Electrochemical measurements were performed using a standard electrical circuit comprising a potentiostat equipped with a programmer (Potentiostat-Galvanostat model 173, EG G Princeton, Applied Research, Princeton, USA), an x-y recorder (Hewlett Packard 7035 B) and a digital voltmeter (Pro's Kit 03-9303 C). The bath contained 0.176 mol dm^{-3} $NiSO_4$, 0.044 mol dm^{-3} $CoSO_4$, 0.005 mol dm^{-3} $CuSO_4$, 3.2 mol dm^{-3} NH_4Cl and 2.3 mol dm^{-3} NH_4OH. The pH of the solution was 10.3 ± 0.1, and was maintained by adding 0.6 mol dm^{-3} NH_4OH. This bath was appropriate because it allowed for the preparation of alloys with specific magnetic properties having a low Cu content (wt%Cu < 3%) and the Ni/Co wt ratio of 5/1. The solution was made up from p.a. chemicals (Merck) and demineralized water. Prior to the recording of polarization curves, the alloy was galvanostatically deposited at 100 mA cm^{-2} for 15 minutes, and then the electrode was transferred to the desired potential. Then, after keeping the electrode for 40 s at the desired potential, the current was recorded. All potentials are expressed relative to the standard hydrogen electrode. The potentials at the polarization

[z] E-mail: smilica84@yahoo.com

curves were corrected for the ohmic potential drop, which was determined by the galvanostatic pulse method. The current efficiency of the alloy deposition was determined by measuring the weight of the alloy deposit and the rate of hydrogen evolution. The time taken for the graduated burette, located above the working electrode, to fill with the evolved hydrogen was measured. Current efficiency was calculated using the mean of four consecutive burette readings. The current for hydrogen evolution was obtained using the equation for Faraday's law applied to the gas evolution process:

$$J\,(H_2) = \frac{nFV_0}{tV_n}$$

Where V_0 is the experimentally determined hydrogen volume at given pressure, p, and temperature, T = 300 K; t is the time of hydrogen evolution under constant current; V_n is the volume of 1 mol of hydrogen under normal conditions (22.4 dm^3 mol^{-1}); n is the number of exchanged electrons and F is Faraday's constant.

The current efficiency of the alloy deposition was then determined using the relation:

$$\eta = \frac{j_{tot} - j_{H_2}}{j_{tot}}.$$

In order to prevent oxidation, upon deposition, the deposits were rinsed four times with 0.1 wt% benzoic acid solution. Then, they were dried in a drier at 105°C.

The chemical composition of the alloy was determined by atomic absorption (Pektar-A-200-Varian). The final composition was the mean of measurements for three deposit samples.

The microstructure of the deposit was calculated by X-ray analysis and DSC thermograms. X-ray diffraction (XRD) was recorded by a Philips PW 1710 diffractometer using CuKα radiation (λ = 0.154 nm) and a graphite monochromator. XRD data were collected with a step size of 0.03° and a collection time of 1.5 s $step^{-1}$. Differential scanning calorimetry (DSC) patterns were obtained on a Shimadzu DSC-50 at a heating rate of 10°C min^{-1} under pure nitrogen flow. Scanning electron microscopy (SEM) analysis was performed by a JEOL-JSM 5300. The size and shape of powder particles were analyzed by a Leica Q500 MC automatic device for microstructural analysis.

Upon heating at a rate of 20°C min^{-1} up to a defined temperature, the alloy sample was cooled to 25°C and then its magnetization was measured. Magnetization was measured by means of a modified Faraday method based on the action of an inhomogeneous field on the magnetic sample. Magnetic force measurements were carried out with a sensitivity of 10^{-6} N in an argon atmosphere.

Results and Discussion

The electrodeposition of Ni-Co-Cu alloys from the ammonium bath was analyzed by recording cyclic voltammograms and polarization curves and by measuring the current efficiency for alloy deposition.

In order to compare the deposition of alloys with and without Cu and analyze the results, cyclic voltammograms for Ni and Co electrodeposition on the titanium substrate from the ammonium solution were recorded (Fig. 1).

The cyclic voltammograms, with the cathodic limits more negative than −0.85 V, exhibit two anodic peaks (I and II) whose maxima shift toward more positive potentials as the cathodic limit potential becomes more negative. If the cathodic limit potential is more positive than −0.80 V, only one anodic peak (I) located at potentials more positive than −0.35 V appears. At potentials more negative than −0.75 V, as the potential is made more negative, the size of peak I does not significantly change. Also, the size of peak I remains unchanged when the potential is stopped for 1.0 to 4.0 minutes at the cathodic limit of −0.75V. Due to the large roughness of the titanium substrate, it is difficult to estimate the value of its real surface area. Therefore, a relatively rough estimate shows that the charge of the first peak corresponds to the formation of one or potentially two monolayers of the Ni-Co alloy on the oxidic titanium surface. This monolayer or

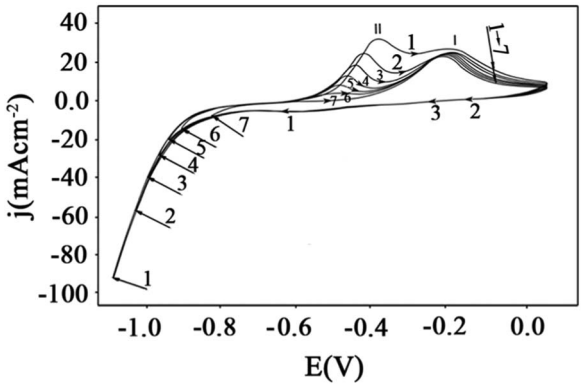

Figure 1. Cyclic voltammograms of Ni-Co alloy electrodeposition from the solution containing 3.2 mol dm^{-3} NH_4Cl, 2.3 mol dm^{-3} NH_4OH, 0.176 mol dm^{-3} $NiSO_4$ and 0.044 mol dm^{-3} $CoSO_4$ at pH = 10.3 and t = 27°C. Sweep rate 50 mV s^{-1}.

these two monolayers are formed owing to the strong interaction of oxidic titanium layer with Ni and Co atoms. It is possible that the first peak is a consequence of the red/ox process on the Ti substrate as well. The second peak is formed by the dissolution of the Ni-Co alloy deposited at potentials more negative than −0.85V. The nickel content of the alloy deposited in this potential range is dependent on the cathodic limit. As the cathodic limit potential is shifted to more negative values i.e. from −0.85V to −1.09V, the nickel content of the alloy increases. The alloy deposited at −0.90V and −0.95V contains 16 ± 0.1% Ni and about 20 ± 1% Ni, respectively. The increase in Ni content causes a shift in peak II maximum potential to more positive values. The considerably narrower ratio of m(Ni)/m(Co) in the alloy than in the solution is an indication of an anomalous codeposition of Ni and Co in this potential range.[14–17,20–37]

Adding 0.005 mol dm^{-3} $CuSO_4$ to the solution has a considerable effect on the electrodeposition of the alloy and, hence, on the chemical composition, morphology, structure and physicochemical properties of the deposit. Figure 2. presents the cyclic voltammograms of Ni-Co-Cu alloy electrodeposition from the ammonium bath on the titanium electrode having different cathodic limits.

The cyclic voltammograms with cathodic limits more negative than −0.98V have three anodic peaks indicated as I, II and III. Peak I exists in the same potential range as peak I in the cyclic voltammograms presented in Figure 1. However, as opposed to peak I in Fig. 1, this peak increases as the potential is stopped at the cathodic limit of −0.75V. This indicates that the deposition of Cu with Ni and Co

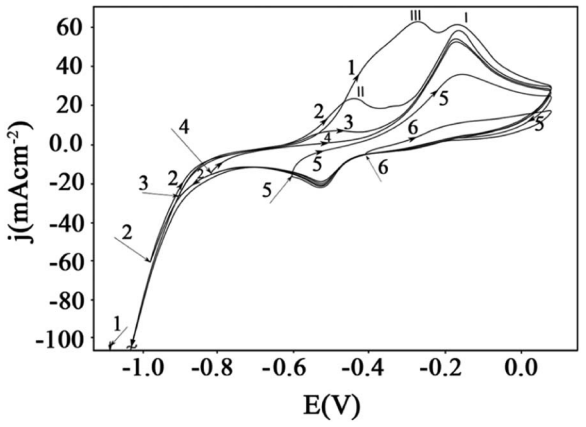

Figure 2. Cyclic voltammograms of Ni-Co-Cu electrodeposition from the solution containing 3.2 mol dm^{-3} NH_4Cl, 2.3 mol dm^{-3} NH_4OH, 0.176 mol dm^{-3} $NiSO_4$, 0.044 mol dm^{-3} $CoSO_4$ and 0.005 mol dm^{-3} $CuSO_4$ at pH = 10.3 and t = 27°C. Sweep rate 50 mV s^{-1}.

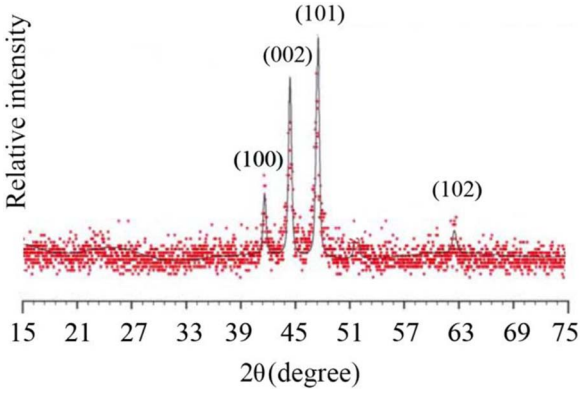

Figure 3. X-ray diffraction pattern of the Co-Ni-Cu alloy electrodeposited at −0.94V from the solution containing 3.2 mol dm^{-3} NH_4Cl, 2.3 mol dm^{-3} NH_4OH, 0.176 mol dm^{-3} $NiSO_4$, 0.044 mol dm^{-3} $CoSO_4$ and 0.005 mol dm^{-3} $CuSO_4$ at pH = 10.3 and t = 27°C.

enables the formation of a multiple deposit which is dissolved at potentials more positive than −0.35 V. The structure of the first peak can be influenced by underpotential codeposition.

Curves 2 and 3 show that the alloy deposited in the potential range of −0.85 V to −0.98V is dissolved during the anodic sweep at potentials between −0.60 V and −0.40 V, causing peak II formation. The X-ray analysis showed that the deposit is composed of an HCP-structured solid solution of Co, Ni and Cu (Fig. 3).

As the electrodeposition potential is shifted to more negative values i.e. from −0.85 V to −0.98 V, the content of Ni in the alloy is increased from about 16 wt% to about 20 wt%, and peak II maximum potentials are shifted to more positive values. If the cathodic limits are more negative than −0.98V, during the anodic sweep, a new peak i.e. peak III is formed. Peak III dominates the cyclic voltammograms obtained after keeping the potential for more than 1.0 minutes at cathodic limits more negative than −1.0V.

The cyclic voltammograms obtained both in the absence and presence of $[Cu(NH_3)_4]^{2+}$ ions (Figs. 1 and 2, respectively) suggest that the co-deposition of copper catalyzes the deposition of the Ni-Co-Cu alloy. This catalytic effect is also confirmed by the polarization curves presented in Fig. 4.

The electrodes with the Cu-containing deposit have greater real surface area than those with the deposit containing no copper. Specifically, during the alloy deposition, copper is co-deposited at the limiting diffusion current at high overpotential, which leads to the rapid formation of nuclei and generation of deposits having large surface areas.[50,59,60]

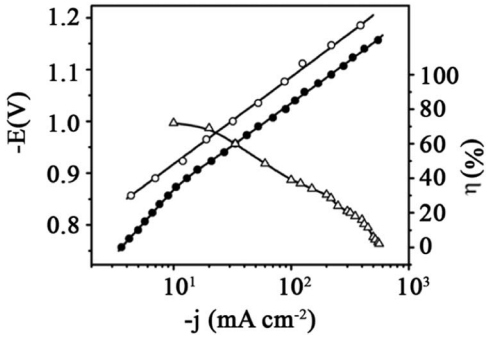

Figure 4. Polarization curves for: ● – Ni-Co-Cu deposition and hydrogen evolution (in the presence of $[Cu(NH_3)_4]^{2+}$) and ○ – Ni-Co deposition and hydrogen evolution (in the absence of $[Cu(NH_3)_4]^{2+}$) and Δ – current efficiency of Ni-Co-Cu alloy as a function of the potential (3.2 mol dm^{-3} NH_4Cl, 2.3 mol dm^{-3} NH_4OH, 0.176 mol dm^{-3} $NiSO_4$, 0.044 mol dm^{-3} $CoSO_4$ and 0.005 mol dm^{-3} $CuSO_4$ at pH = 10.3 and t = 27°C).

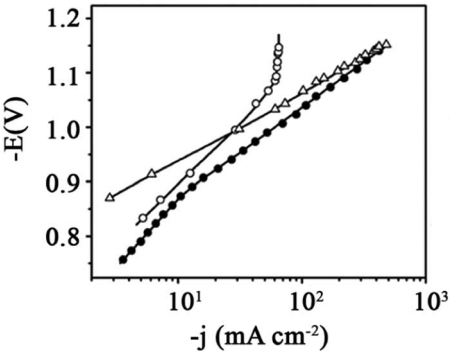

Figure 5. Cathodic polarization curves: ● – total cathodic polarization curve; ○ – polarization curve for Ni-Co-Cu alloy deposition; Δ – polarization curve for hydrogen evolution (3.2 mol dm^{-3} NH_4Cl, 2.3 mol dm^{-3} NH_4OH, 0.176 mol dm^{-3} $NiSO_4$, 0.044 mol dm^{-3} $CoSO_4$ and 0.005 mol dm^{-3} $CuSO_4$ at pH = 10.3 and t = 27°C).

The current efficiencies of alloy deposition decrease with increasing current density. At the same current density, the current efficiencies of the copper-containing alloy are higher by about 12% than those of the alloy without copper. This is mostly due to the lower current density with respect to the real surface area of the copper-containing deposit i.e. due to the greater real surface area of the copper-containing deposit than of the deposit without copper. In addition, the copper present on the surface of the alloy, due to the high overpotential value for hydrogen evolution, also causes a partial increase in the current efficiency of the alloy.

The total polarization curve and current efficiencies for alloy deposition were used to determine partial polarization curves for alloy deposition and hydrogen evolution (Fig. 5).

The Tafel slope of hydrogen evolution is 129 mV. The deposition of Ni and Co is activation-controlled up to the partial current density of about 20 mA cm^{-2}. In the current density range of 20–65 mA cm^{-2}, this deposition is a mixed activation/diffusion controlled process. At potentials more negative than −1.09V, a limiting diffusion current for Ni-Co-Cu alloy deposition is established.

The effect of total current density on the chemical composition of the deposit was investigated. The obtained values are presented in Table I.

As shown, the chemical compositions of the deposits obtained in the total cathodic current density range of 100–400 mA cm^{-2} are not significantly dependent on current density. In this range, there is no significant difference in the chemical composition of the deposits since the deposition of all three metals occurs at limiting or approximately limiting diffusion currents.

The microstructure, morphology and magnetic properties of the $Ni_{79.1}Co_{18.6}Cu_{2.3}$ powder obtained at the current density of j = 100 mA cm^{-2} were analyzed in detail. The phase structure was determined by XRD analysis. Figure 6. presents X-ray diffraction patterns of as-obtained and annealed powders.

The diagram shows only peaks for the (111), (200), (220) and (311) planes of FCC crystals of the solid solution of cobalt and copper in nickel. There are no peaks for pure metals and their oxides and

Table I. Chemical compositions of deposits obtained by the electrolysis of the solution containing 3.2 mol dm^{-3} NH_4Cl, 2.3 mol dm^{-3} NH_4OH, 0.176 mol dm^{-3} $NiSO_4$, 0.044 mol dm^{-3} $CoSO_4$ and 0.005 mol dm^{-3} $CuSO_4$ at pH = 10.3 and t = 27°C.

J mA cm^{-2}	Ni wt%	Co wt%	Cu wt%
100	79.13	18.54	2.33
155.6	79.00	18.79	2.21
200	79.68	18.76	1.56
400	79.71	18.73	1.56

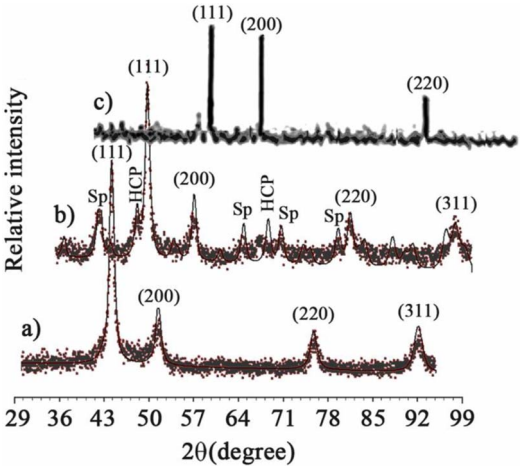

Figure 6. X-ray diffraction patterns of $Ni_{79.1}Co_{18.6}Cu_{2.3}$ powder deposited at 100 mA cm^{-2} from the solution containing 3.2 mol dm^{-3} NH_4Cl, 2.3 mol dm^{-3} NH_4OH, 0.176 mol dm^{-3} $NiSO_4$, 0.044 mol dm^{-3} $CoSO_4$ and 0.005 mol dm^{-3} $CuSO_4$ at pH = 10.3 and t = 27°C. a – as-deposited powder; b – powder annealed for 30 minutes at 300°C and c – powder annealed for 30 minutes at 450°C.

intermetallic compounds, nor are there peaks for the HCP phase of the solid solution of nickel and copper in cobalt. The peaks are relatively wide, low in intensity and shifted toward lower 2θ values compared to the values for the pure nickel FCC phase. This indicates that the powder contains small crystalline grains with a high minimum density of chaotically distributed dislocations and a high internal microstrain value, as illustrated in Table II.

The powders having the same nickel to cobalt ratio and no copper, obtained from the ammonium solution at the same current density and at the same temperature, were found to have much larger crystals.[49] The incorporation of Cu into the deposited FCC-structured solid solution of Co in Ni causes the formation of smaller nanocrystals having a high mean microstrain value and a high density of chaotically distributed dislocations.[49,50] The overpotential for Cu deposition at Ni-Co-Cu alloy deposition current densities higher than 100 mA cm^{-2} is high. At high overpotentials, the critical radius of the nucleus and the number of atoms in the critical nucleus is smaller than at low overpotentials. Therefore, the induction time for nucleus formation exponentially decreases with increasing deposition overpotential. As the result, during the deposition of Ni-Co alloy with Cu, the nucleus formation rate is considerably higher and, hence, the number of nuclei on the deposit surface is considerably larger than during the deposition of Ni and Co without copper. The greater density of nuclei on the deposit surface causes the formation of smaller crystalline grains, which exhibit higher internal microstrain values and a higher density of chaotically distributed dislocations.[49,50,59,60] As the mean nanocrystal size decreases, the mass percentage of the amorphous matrix located between the nanocrystals increases.[61–64] Therefore, Ni/Co electrodeposits with Cu have a larger amount of the amorphous phase compared to those without copper.

The highest (111) peak intensity indicates texture existence. The development of this texture is associated with the preferred growth along (111) orientation due to the lower strain associated in that direction.[60–63] The ratio of the relative integrated intensity of the (111) peak to that of the (200) peak of the FCC phase of the powder electrodeposited at j = 100 mA cm^{-2} is the same as the ratio of the relative integrated intensities of the (111) peak to the (200) peak of the nickel polycrystal obtained by powder metallurgy. This suggests that the strain is distributed in different directions as in the randomly textured nickel polycrystal. The low mean crystallite size value, 6.8 nm, suggests that $Ni_{79.1}Co_{18.6}Cu_{2.3}$ powder contains not only nanocrystals, but also an amorphous phase. The presence of both the amorphous phase and the nanocrystalline phase in electrodeposited powders has also been reported elsewhere.[61–64] Transmission electron microscopic observations of electrodeposited Ni-W binary alloys have also shown the distribution of nanocrystals in an amorphous matrix.[64]

Annealing nanostructured alloys at elevated temperatures changes their microstructure and, hence, their physicochemical characteristics.

$Ni_{79.1}Co_{18.6}Cu_{2.3}$ alloy samples were annealed at 160°C, 200°C and 260°C for 30 minutes in an argon atmosphere. Thereafter, they were cooled to room temperature and, then, their diffraction patterns were recorded. The obtained diffractograms were identical to those of as-prepared samples. This indicated that no phase transformations took place in the samples during annealing at temperatures up to 260°C. There are small differences between the diffraction pattern of the alloy annealed at 300°C and that of the as-prepared sample (Fig. 6b). The microstructural changes determined from the diffraction pattern are presented in Table II. As shown in the table, during annealing at 300°C, the minimum density of chaotically distributed dislocations and the mean microstrain value decreased, whereas the mean crystallite size slightly increased. This indicates that, at this temperature, the alloy undergoes structural relaxation and short-range ordering. The small increase in crystalline grain size is probably due to short-range ordering in the thin part of the amorphous layer next to the crystalline grains. In this part of the amorphous layer, there is the highest level of structural order; therefore, a relatively small amount of ordering is sufficient to transform it into the crystalline phase. The diffraction pattern (Fig. 6b) also shows weak peaks of the HCP phase of the solid solution of cobalt, nickel and copper, with $P6_3/mmc$ symmetry and the unit cell parameters a = b = 0.24470(6) nm, c = 0.4094 (1) nm, α = β = 90° and γ = 120°C. The traces of oxygen present in the furnace enabled the formation of a small amount of $Ni_{79.1-x}Co_{18.6-y}O_{x+y}$ oxide having a spinel structure (Sp) with Fd–3 m symmetry and the unit cell parameters a = b = c = 0.80926(9) nm and α = β = γ = 90°C.

The samples annealed at 450°C exhibit only prominent peaks of the FCC phase of the solid solution of Co and Cu in Ni. The intensity of these peaks is considerably higher and their width at half height smaller than in unannealed powder samples (Fig. 6c). This is the result of amorphous phase crystallization and FCC crystalline growth, accompanied by decreases in internal microstrain and minimum density of chaotically distributed dislocations (Table II). The presence of the amorphous phase in the as-deposited powder and its crystallization during annealing are confirmed by the increase in the ratio of the relative integrated intensities of the (111) and (200) peaks of the FCC phase of annealed vs. unannealed powders. The diffraction

Table II. Microstructural data for $Ni_{79.1}Co_{18.6}Cu_{2.3}$ powder.

Crystal structure	Unit cell parameters (nm)	Mean crystallite size value (nm)	Mean microstrain value	Minimum density of chaotically distributed dislocations (cm^{-2})
		as-deposited powder		
FCC	a = 0.35505(4)	6.8	$3.1 \cdot 10^{-3}$	$6.5 \cdot 10^{12}$
		powder annealed for 30 minutes at 300°C		
FCC	a = 0.35420(5)	8.9	$2.5 \cdot 10^{-3}$	$3.7 \cdot 10^{12}$
		powder annealed for 30 minutes at 450°C		
FCC	a = 0.35360(4)	17.1	$1.8 \cdot 10^{-3}$	$1.0 \cdot 10^{12}$

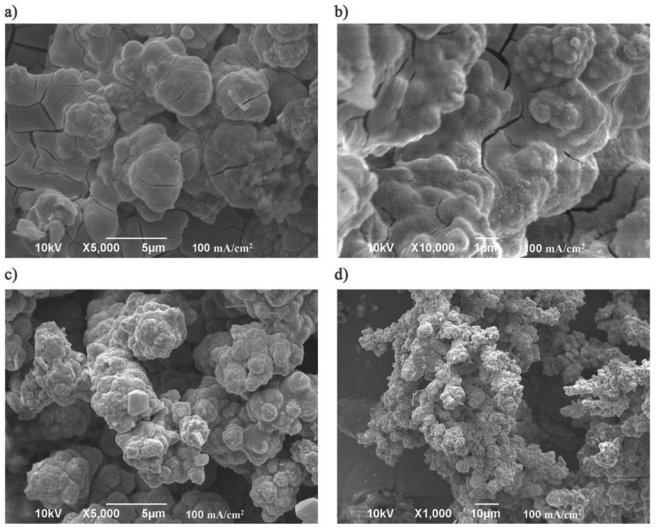

Figure 7. SEM micrographs of $Ni_{79.1}Co_{18.6}Cu_{2.3}$ powder electrodeposited at 100 mA cm^{-2} from the solution containing 3.2 mol dm^{-3} NH_4Cl, 2.3 mol dm^{-3} NH_4OH, 0.176 mol dm^{-3} $NiSO_4$, 0.044 mol dm^{-3} $CoSO_4$ and 0.005 mol dm^{-3} $CuSO_4$ at pH = 10.3 and t = 27°C.

pattern of the alloy annealed at 450°C shows very weak peaks of the $Ni_{19.1-x}Co_{18.6-y}O_{x+y}$ cubic phase.

SEM images show that the $Ni_{79.1}Co_{18.6}Cu_{2.3}$ alloy powder electrodeposited at j = 100 mA cm^{-2} is composed of two shapes of particles: large cauliflower-like particles and small dendritic ones (Fig. 7). Dendritic particles have a high density of secondary branches and higher-order branches. The density of branches is considerably greater in dendrites of $Ni_{79.1}Co_{18.6}Cu_{2.3}$ powder than in those of powders without copper ($Ni_{80}Co_{20}$), due to the higher rate of nucleation during the alloy deposition in the presence of Cu^{2+} ions than in their absence.[59,60]

Dendrites are made up of a series of interconnected globules.[40,59,60] Secondary and higher-order branches form angles of mostly 30–90° with the main branch. Globular branches are formed because, after nucleus formation, spherical diffusion is established in a relatively short period of time. Before globules are transformed into needle-like crystals, new nuclei are formed at the tips of globules and are transformed into new globules over time. This process involving the formation of new globules continues, resulting in the formation of globular branches. At the same time, nuclei are formed on the sides of branches, and are transformed into globules. Then, the formation of a series of globules on these lateral globules results in the formation of lateral branches. When the number of branches reaches the critical value, globules at the tips of branches merge to form a cauliflower. Thereafter, new globules are formed on the rough cauliflower surface (Fig. 7). The appearance of a large number of cracks indicates that the deposit has high internal microstrain values (Fig. 7). There are craters at some places on the deposit particle surface. These are hydrogen evolution sites. Gas bubbles at these places prevent the deposition of metals. There are needle-like dendrites at the bottom of some craters. Bubbles evolved from these craters before the powder separated from the cathode. The dendrites are needle-like crystals since planar diffusion takes place in the crater. There are no dendrites in the craters from which no bubbles evolved before the separation of the powder from the cathode.

The deposition of copper with nickel and cobalt affects the particle size and shape of the powder. The copper-containing powder has smaller and more rounded particles compared to the copper-free powder having the same weight ratio of Ni to Co, obtained at the same current density. Copper co-deposition enhances the formation of nuclei and generation of a higher density of higher-order branches and, hence, the formation of smaller cauliflower-shaped particles with a higher density of smaller semi-globules on the surface. Due to the higher rate of nucleation, Cu-containing deposits are formed in powdered form at lower current densities compared to the deposits without Cu. For the sake of illustration, cumulative curves for maximum and minimum particle size distribution and histograms of the relative frequency distribution of maximum and minimum particle sizes of $Ni_{79.1}Co_{18.6}Cu_{2.3}$ alloy powder are presented in Fig. 8.

The physicochemical properties of the electrodeposited alloys are dependent on the kinetic and operational parameters of electrolysis, as well as on the temperature and time of subsequent annealing. Annealing the as-deposited alloys changes their microstructure and, hence, their mechanical, electrical and magnetic properties.[49,50,59,60] In this research, the effect of annealing temperature on the magnetic properties of $Ni_{79.1}Co_{18.6}Cu_{2.3}$ alloy was investigated. As shown in Figure 9, the relative permeability μ_t/μ_{20} of the alloy cooled at 20°C remains unchanged after annealing in the temperature range of 20–160°C. This confirms that, during annealing, in this temperature range, no structural changes occur in the as-deposited $Ni_{79.1}Co_{18.6}Cu_{2.3}$ alloy.

As the annealing temperature increases in the temperature range 160–640°C, the relative magnetic permeability of the powder cooled at 20°C increases, reaching its maximum at 430°C and then decreases. This change in magnetic permeability is due to structural changes.

Differential scanning calorimetry, DSC, was used to evaluate the effect of annealing temperature on structural changes (Fig. 10). As shown in the DSC image, there are no pronounced peaks in the temperature range of 20–160°C, which also confirms that, during annealing, the powder does not undergo structural changes in this temperature range.

At temperatures ranging from 160°C to 350°C, there are several weak exo-peaks. The existence of these exo-peaks and the fact that XRD patterns of the alloys annealed in this temperature range are approximately the same as those of the as-obtained powder indicate that structural relaxation takes place in the temperature range 160–350°C. Therefore, the increase in magnetization during annealing at temperatures between 160°C and 350°C is due to structural relaxation.

The electrodeposition of the nickel-cobalt-copper alloy does not produce an ideal amorphous phase with a completely random distribution of spacings between adjacent atoms; it leads to the formation of a phase with more or less short-range ordered atoms.[65,66] During annealing in the temperature range of 160–350°C, the as-prepared $Ni_{79.1}Co_{18.6}Cu_{2.3}$ alloy undergoes short-range ordering in both the amorphous phase and nanocrystals, accompanied by concurrent decreases in internal microstrain and density of chaotically distributed dislocations in the FCC phase. Through the effect of heat, metal atoms drop from higher energy levels across the energy barrier down to lower energy levels, where their 3d and 4 s orbitals overlap more effectively with the orbitals of adjacent atoms of the same type and symmetry, thus increasing the exchange integral value and the electron density of states near the Fermi level.[49,50,59,60] The atoms arriving at lower energy levels adjoin energetically more favorable domains. The decrease in the minimum density of chaotically distributed dislocations, resulting from structural relaxation, enhances the mobility of magnetic domain walls and facilitates the orientation of these domains in the external magnetic field. This causes domain expansion and an increase in magnetization.

In the temperature range of 350–430°C, as the annealing temperature increases, the magnetization of powders cooled at 25°C increases (Fig. 9). The thermogram shows the appearance of an exothermic shoulder at 430°C and an exothermic maximum at 540°C. The appearance of the exothermic shoulder is most likely due to the crystallization of the amorphous phase, which exhibits relatively lower magnetic permeability, and the resulting formation of smaller nanocrystalline grains of the FCC-structured solid solution, which has considerably higher magnetic permeability. Therefore, this process causes an increase in relative magnetic permeability. The appearance of the exothermic maximum at 540°C is attributed to the growth of larger FCC crystalline grains at the expense of smaller ones. The formation of larger crystalline grains during annealing in the temperature range 430–550°C causes a decline in the magnetization of samples cooled at 25°C. The abrupt decline in the magnetization of samples cooled at 25°C with increasing annealing temperature in the temperature range

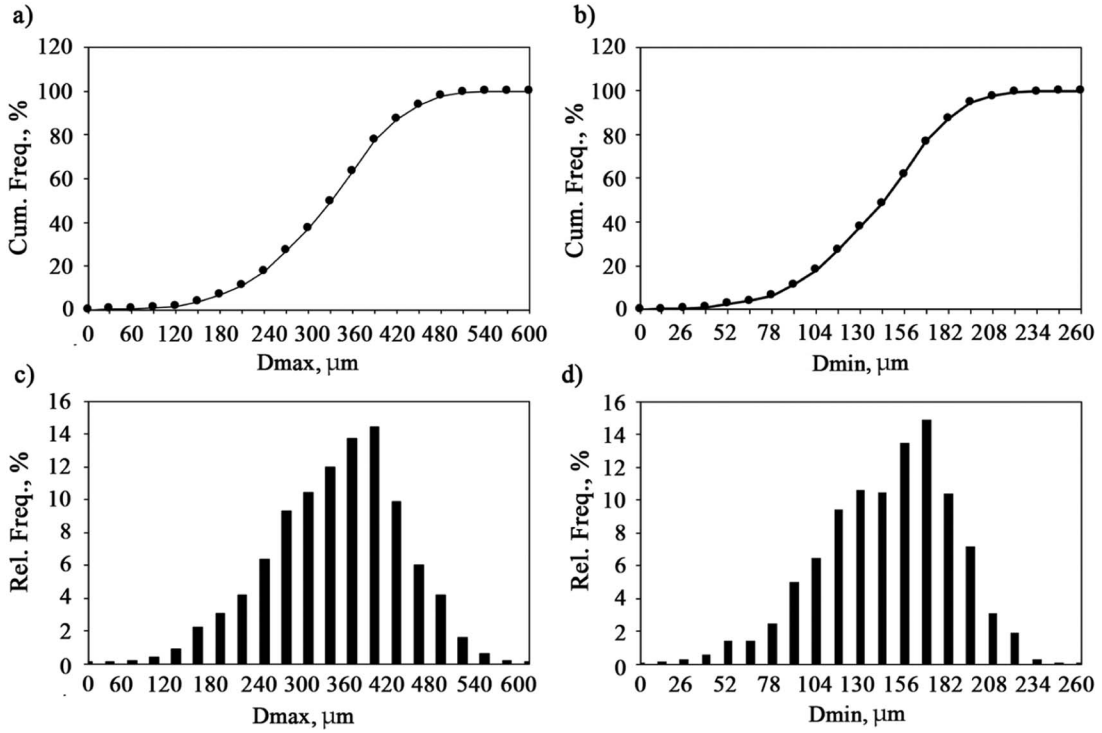

Figure 8. Cumulative curves for the distribution of a) maximum particle size, Dmax, and b) minimum particle size, Dmin, and c) – histograms of the relative frequency distribution of maximum particle sizes, Dmax, and d) – minimum particle sizes, Dmin, of $Ni_{79.1}Co_{18.6}Cu_{2.3}$ alloy powder electrodeposited at j = 100 mA cm^{-2} (3.2 mol dm^{-3} NH_4Cl, 2.3 mol dm^{-3} NH_4OH, 0.176 mol dm^{-3} $NiSO_4$, 0.044 mol dm^{-3} $CoSO_4$ and 0.005 mol dm^{-3} $CuSO_4$ at pH = 10.3 and t = 27°C).

550–700°C is due to the relatively rapid formation of considerably larger crystalline grains at higher temperatures. Larger crystalline grains hamper the orientation of some magnetic domains and reduce the mobility of walls of already oriented domains.[13,14,22,26,29,35–38]

The results show that the electrodeposition from an ammonium sulfate bath can produce Ni-Co powders containing a small amount of Cu, with high current efficiencies, exhibiting the desired particle size and chemical composition, specific microstructure and good magnetic characteristics.

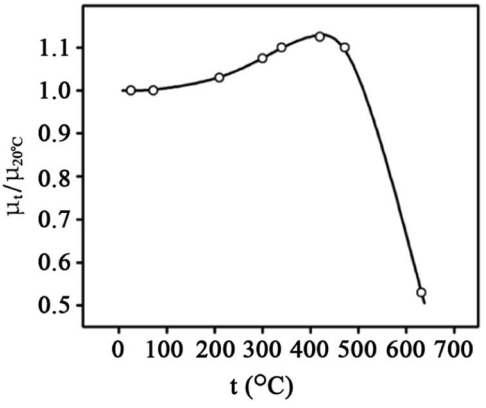

Figure 9. A relative change in the magnetic permeability μ_t/μ_{20} of $Ni_{79.1}Co_{18.6}Cu_{2.3}$ alloy powder cooled at 20°C as a function of previous annealing temperature, t. The powder was first annealed at the heating rate of 20°C min^{-1} to a final temperature, and then annealed at the final temperature for 15 minutes. The powder was electrodeposited at j = 100 mA cm^{-2} from the solution containing 3.2 mol dm^{-3} NH_4Cl, 2.3 mol dm^{-3} NH_4OH, 0.176 mol dm^{-3} $NiSO_4$, 0.044 mol dm^{-3} $CoSO_4$ and 0.005 mol dm^{-3} $CuSO_4$ at pH = 10.3 and t = 27°C.

Conclusions

Powders of Ni-Co alloys containing small amounts of Cu were produced by electrodeposition from an ammonium bath at room temperature. Electrochemical characteristics were determined by recording cyclic voltammograms, the polarization curve and current efficiency for alloy deposition. The current efficiency was found to decrease with increasing current density. Alloy deposition at potentials more negative than −1.09V takes place at the limiting diffusion current. In the total cathodic current range of 100 to 400 mA cm^{-2}, where Ni, Co and Cu are co-deposited at the limiting diffusion current, the chemical composition of the powder does not practically depend on current density. The $Ni_{79.1}Co_{18.6}Cu_{2.3}$ powder obtained at 100 mA cm^{-2} is composed of an amorphous matrix and nanocrystals with an average size of 6.8 nm of the FCC-structured solid solution of Co and

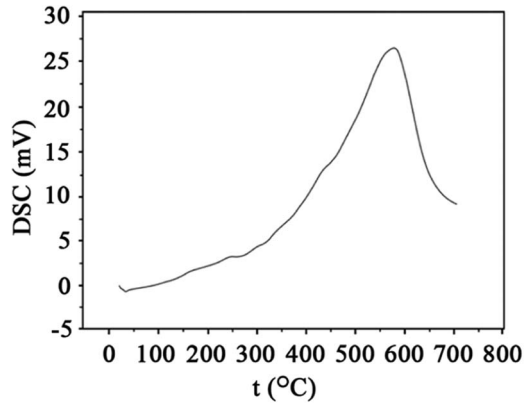

Figure 10. DSC pattern for $Ni_{79.1}Co_{18.6}Cu_{2.3}$ powder electrodeposited at j = 100 mA cm^{-2} from the solution containing 3.2 mol dm^{-3} NH_4Cl, 2.3 mol dm^{-3} NH_4OH, 0.176 mol dm^{-3} $NiSO_4$, 0.044 mol dm^{-3} $CoSO_4$ and 0.005 mol dm^{-3} $CuSO_4$ at pH = 10.3 and t = 27°C. Heating rate 10°C min^{-1}.

Cu in Ni. Powder particles are cauliflower-shaped or dendritic with a large number of secondary and higher-order branches. The deposition of Co with Ni and Co causes a higher percentage of the amorphous phase, smaller nanocrystals, and smaller and more rounded particles of Ni-Co-Cu alloy powders than the deposition of the alloy without Cu.

DSC and XRD measurements showed that, during annealing in the temperature range of 25 to 160°C, no structural changes take place in the powder. However, during annealing at temperatures between 160°C and 350°C, irreversible structural relaxation occurs in the alloy, involving short-range ordering, accompanied by a decrease in internal microstrain and a decrease in the density of chaotically distributed dislocations, resulting in increased magnetic permeability of the cooled samples. In the temperature range of 350 to 430°C, the amorphous phase, which exhibits relatively lower magnetization, is crystallized, and small FCC nanocrystals of the solid solution of Co and Cu in Ni, having considerably higher magnetization, are formed. These changes in this temperature range cause an increase in the magnetic permeability of samples cooled at 25°C with increasing annealing temperature. At temperatures above 430°C, the formation of large crystalline grains at the expense of smaller ones causes a decrease in magnetization.

The results show that the proper choice of kinetic and operational electrodeposition parameters can result in the obtainment of the desired particle size and chemical composition, microstructure and magnetic characteristics of powders of Ni-Co alloys containing small amounts of Cu deposited from an ammonium solution.

Acknowledgment

This work was supported by the Ministry of Education and Science of the Republic of Serbia through Project Ref. No. 172057.

ORCID

Milica Spasojević https://orcid.org/0000-0001-9134-6637

References

1. S. Steeb and H. Warlimont, *Rapidly Quenched Metals*, Elsevier, Amsterdam, 1 (1985).
2. R. Salvio, J. Huskens, and D. Reinhoudt, in D. L. Andrews, G. D. Scholes, and G. P. Wiederrecht, (eds.), *Comprehensive Nanoscience and Technology*, **4**(4.06) 145 (2011).
3. G. Panthi, M. Park, H. Y. Kim, and S. J. Park, *Journal of Industrial and Engineering Chemistry*, **24**, 1 (2015).
4. M. A. Augustin and P. Sanguansri, *Adv. Food Nutr. Res.*, **58**, 183 (2009).
5. Z. Tang, C. He, H. Tian et al., *Progress in Polymer Science*, **60**, 86 (2016).
6. L. Gunther, *Phys. World*, **3**, 28 (1990).
7. P. Toneguzzo, G. Viau, O. Acher, F. Fiévet-Vincent, and F. Fiévet, *Adv. Mater.*, **10**, 1032 (1998).
8. G. Viau, F. Fiévet-Vincent, and F. Fiévet, *Solid State Ionics*, **84**, 259 (1996).
9. F. Fievet, J. P. Lagier, and M. Figlarz, *MRS Bulletin*, **14**, 29 (1989).
10. P. Toneguzzo, *Ph.D. Thesis*, Laboratoire de Chimie des Matériaux Divisés et Catalyse, Université Paris 7, France, Denis Diderot (1997).
11. K. V. M. Shafi, A. Gedanken, and R. Prozorov, *J. Mater. Chem.*, **8**, 769 (1998).
12. Y. D. Li, L. Q. Li, H. W. Liao, and H. R. Wang, *J. Mater. Chem.*, **9**, 2675 (1999).
13. P. Elumalai, H. N. Vasan, M. Verelst, P. Lecante, V. Carles, and P. Tailhades, *Mat. Res. Bull.*, **37**, 353 (2002).
14. C. Ma, S. C. Wang, and F. C. Walsh, *Transactions of the IMF*, **93**, 104 (2015).
15. C. Ma, S. C. Wang, C. T. J. Low, L. P. Wang, and F. C. Walsh, *Transactions of the IMF*, **92**, 189 (2014).
16. C. Ma, S. C. Wang, and F. C. Walsh, *Transactions of the IMF*, **93**, 8 (2015).
17. L. Wang, Y. Gao, Q. Xue, H. Liu, and T. Xu, *Appl. Surf. Sci.*, **242**, 326 (2005).
18. A. Bai and C. C. Hu, *Electrochim. Acta*, **50**, 1335 (2005).
19. C. Liu, F. Su, and J. Liang, *Surf. Coat. Tech.*, **292**, 37 (2016).
20. D. S. Schweckandt and M. del C. Aguirre, *Pr. Mater. Sci.*, **8**, 91 (2015).
21. L. Tian, J. Xu, and C. Qiang, *App. Surf. Sci.*, **257**, 4689 (2011).
22. L. Tian, J. Xu, and S. Xiao, *Vacum*, **86**, 27 (2011).
23. Y. Li, H. Jiang, W. Huang, and H. Tian, *Appl. Surf. Sci.*, **254**, 6865 (2008).
24. A. Karpuz, H. Kockar, M. Alper, O. Karaagac, and M. Haciismailoglu, *Appl. Surf. Sci.*, **258**, 4005 (2012).
25. A. Karpuz, H. Kockar, and M. Alper, *Appl. Surf. Sci.*, **258**, 5046 (2012).
26. C. Lupi, A. Dell'Era, M. Pasquali, and P. Imperatori, *Surf. Coat. Tech.*, **205**, 5394 (2011).
27. J. Y. Li, C. Ni, J. Y. Liu, M. J. Jin, W. Li, and X. J. Jin, *Mater. Chem. Phys.*, **148**, 1202 (2014).
28. O. Ergeneman, K. M. Sivaraman, S. Pané, E. Pellicer, A. Teleki, A. M. Hirt, M. D. Baró, and B. J. Nelson, *Electrochim. Acta*, **56**, 1399 (2011).
29. S. Khorsand, K. Raeissi, F. Ashrafizadeh, M. A. Arenas, and A. Conde, *Appl. Surf. Sci.*, **364**, 349 (2016).
30. C. K. Chung and W. T. Chang, *Thin Solid Films*, **517**, 4800 (2009).
31. J. Vazquez-Arenas, L. Altamirano-Garcia, T. Treeratanaphitak, M. Pritzker, R. Luna-Sánchez, and R. Cabrera-Sierra, *Electrochim. Acta*, **65**, 234 (2012).
32. A. Karpuz, H. Kockar, and M. Alper, *J. Mag. Mag. Mater.*, **373**, 115 (2015).
33. M. Zamani, A. Amadeh, and S. M. Lari Baghal, *Transactions of Nonferrous Metals Society of China*, **26**, 484 (2016).
34. Q. S. Chen, Z. Y. Zhou, G. C. Guo, and S. G. Sun, *Electrochim. Acta*, **113**, 694 (2013).
35. S. Olvera, E. M. Arce Estrada, J. Sanchez-Marcos, F. J. Palomares, L. Vazquez, and P. Herrasti, *Mater. Charact.*, **105**, 136 (2015).
36. Y. Li, H. Jiang, D. Wang, and H. Ge, *Surf. Coat. Tech.*, **202**, 4952 (2008).
37. D. M. Dryden, T. Sun, R. McCormick, R. Hickey, R. Vidu, and P. Stroeve, *Electrochim. Acta*, **220**, 595 (2016).
38. L. D. Rafailović, H. P. Karnthaler, T. Trišović, and D. M. Minić, *Mater. Chem. Phys.*, **120**, 409 (2010).
39. V. D. Jović, B. M. Jović, and M. G. Pavlović, *Electrochim. Acta*, **51**, 5468 (2006).
40. V. M. Maksimović, U. Č. Lačnjevac, M. M. Stoiljković, M. G. Pavlović, and V. D. Jović, *Mater. Charact.*, **62**, 1173 (2011).
41. B. P. Yur'ev and L. A. Golubkov, *Trudy–Leningradskii Politekhnicheskii Institut imeni M. I. Kalinina*, **14**, 269 (1969).
42. A. M. Abd El-Halim and R. M. Khalil, *Surf. Coat. Technol.*, **27**, 103 (1986).
43. V. D. Jović, B. M. Jović, M. G. Pavlović, and V. Maksimović, *J. Solid. State. Electrochem.*, **10**, 959 (2006).
44. V. D. Jović, B. M. Jović, M. V. Maksimović, and G. Pavlović, *Electrochim. Acta*, **52**, 4254 (2007).
45. V. D. Jović, V. Maksimović, M. G. Pavlović, and K. I. Popov, *J. Solid. State. Electrochem.*, **10**, 373 (2006).
46. S. Randjić, A. Maričić, L. Rafailović, M. Spasojević, and M. M. Ristić, *Sci. Sinter.*, **38**, 139 (2006).
47. A. Maričić, M. Spasojević, S. Arnaut, D. Minić, and M. M. Ristić, *Sci. Sinter.*, **40**, 303 (2008).
48. R. Simeunović, A. Maričić, A. Kalezić-Glišović, and M. Spasojević, *Sci. Sinter.*, **38**, 283 (2006).
49. M. Spasojević, L. Ribić-Zelenović, and A. Maričić, *Sci. Sinter.*, **43**, 313 (2011).
50. M. Spasojević, A. Maričić, L. Ribić Zelenović, N. Krstajić, and P. Spasojević, *J. Alloy. Comp.*, **551**, 660 (2013).
51. Salvador Pané, Elvira Gómez, and Elisa Vallés, *J. Electroanal. Chem.*, **596**, 87 (2006).
52. D. M. Davis and E. J. Podlaha, *Electrochem. Solid-State Lett.*, **8**, D1 (2005).
53. E. Gómez, S. Pané, and E. Vallés, *Electrochim. Acta*, **51**, 146 (2005).
54. A. P. O'Keeffe, O. I. Kasyutich, W. Schwarzacher, L. S. de Oliveira, and A. A. Pasa, *Appl. Phys. Lett.*, **73**, 1002 (1998).
55. O. I. Kasyutich, W. Schwarzacher, V. M. Fedosyuk, P. A. Laskarzhevskiy, and A. I. Masliy, *J. Electrochem. Soc.*, **147**(8), 2964 (2000).
56. G. Nabiyouni, O. I. Kasyutich, S. Roy, and W. Schwarzacher, *J. Electrochem. Soc.*, **149**(4), C218 (2002).
57. G. Nabiyouni, W. Schwarzacher, Z. Rolik, and I. Bakonyi, *J. Magn. Magn. Mater.*, **253**(1–2), 77 (2002).
58. S. M. S. I. Dulal, E. A. Charles, and S. Roy, *Electrochim. Acta*, **49**, 2041 (2004).
59. M. Spasojević, A. Maričić, Z. Vuković, S. Đukić, L. Ribić-Zelenović, and M. Spasojević, *J. Nanomater.*, **2017**, ID 8230615 (2017).
60. M. Spasojević, D. Gospavić, and M. Spasojević, *J. Electrochem. Soc.*, **163**(14), D842 (2016).
61. K. R. Sriraman, S. Ganesh Sundara Raman, and S. K. Seshadri, *Mater. Sci. Technol.*, **22**, 14 (2006).
62. K. R. Sriraman, S. Ganesh Sundara Raman, and S. K. Seshadri, *Mater. Sci. Eng., A*, **418**, 303 (2006).
63. N. Ćirović, P. Spasojević, L. Ribić-Zelenović, P. Mašković, and M. Spasojević, *Science of Sintering*, **47**, 347 (2015).
64. T. Yamasaki, *Scripta Materialia*, **44**, 1497 (2001).
65. K. E. Heusler and D. Huerta, *J. Electrochem. Soc.*, **136**, 65 (1989).
66. M. Donten, *J. Solid State Electrochem.*, **3**, 87 (1999).